

A Compound Control Strategy for Improving the Dynamic Characteristics of the DC-Link Voltage for the PMSM Drive System Based on the Quasi-Z-Source Inverter

DONG SHUAI^{ID}, ZHANG QIANFAN, ZHANG WEIPAN, ZHOU CHAOWEI, AND NA TUOPU

School of Electrical Engineering and Automation, Harbin Institute of Technology, Harbin 150000, China

Corresponding authors: Dong Shuai (dongshuai@hit.edu.cn) and Zhang Qianfan (zhang_qianfan@hit.edu.cn)

This work was supported in part by the Fundamental Research Funds for the Central Universities under Grant HIT.NSRIF.2019022, and in part by the China Postdoctoral Science Foundation under Grant 2018T110297 and Grant 2017M621271.

ABSTRACT The promising quasi-Z-Source inverter (qZSI) can regulate the DC-link voltage. In the study, a permanent magnet synchronous motor (PMSM) drive system is established with the qZSI. Based on the small-signal model, a feedback and feedforward compound control strategy is proposed and the dynamic performance of the converter is analyzed. The simulation and experimental results indicate that the compound control strategy effectively improves the static and dynamic characteristics of the DC-link voltage and reduces the influence of power variation on the DC-link voltage.

INDEX TERMS Quasi-Z-Source inverter, DC-link voltage, PMSM, control strategy.

I. INTRODUCTION

A traditional motor drive system generally uses the battery plus voltage source inverter (VSI) to supply power [1], [2]. In order to raise the DC bus voltage, a cascaded DC-DC converter is often provided between the battery and the inverter [3]. In the system, the upper and lower switches of the same bridge arm cannot be turned on simultaneously. However, under complex working conditions, various disturbances may cause the switch mis-conduction and impair the reliability of the converter. To avoid the shoot-through state, it is necessary to add dead time, which brings out impulses in motor torque and harmonic loss increment and decreases the whole efficiency [4], [5].

The Z-Source inverter (ZSI) can function as both booster and inverter and replace the cascade system composed of the DC-DC converter and the VSI [6]. In addition, it can adjust the DC-link voltage and allow the shoot-through state. Compared with cascaded DC-DC systems, the ZSI is a single-stage system with higher reliability. However, it has

the disadvantages of high voltage stress and discontinuous input current.

Various impedance source inverters have been proposed. The trans-ZSI [7] and Γ -ZSI [8] replace traditional ZSI inductors with double-winding transformer and reduce the number of capacitors to one. The trans-ZSI inverter maintains the high voltage boosting ability while ensuring the advantage of low voltage stress. With the increase in the shoot-through ratio, the voltage boosting ability of the Γ -ZSI gradually decreases. T-ZSI [9] adopts the double-winding inductance coupling technology, which also reduces the numbers of inductors and capacitors to one. Since the passive devices and inverters share a common DC source, this impedance network is suitable for the application of multilevel NPC inverters. Although the impedance source inverters utilizing transformer or inductor coupling technology reduce the number of inductors and capacitors, it is difficult to avoid the voltage spike effects caused by leakage inductance. Switching inductors composed of two inductors and three diodes have the advantage of high boost ratio, such as SL-qZSI [10] and SL-ZSI [11]. During the transition from shoot-through state to non-shoot-through state, the two inductors are converted from parallel charge to series discharge to realize the purpose of high voltage

The associate editor coordinating the review of this manuscript and approving it for publication was Yuh-Shyan Hwang.

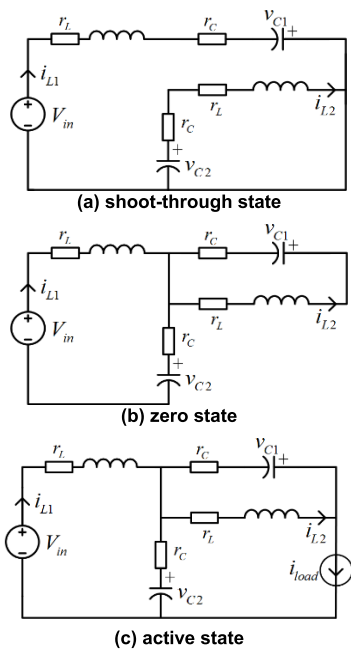


FIGURE 3. Equivalent topology.

has the upper and lower switches turned on simultaneously, known as bridge arm short circuit. Generally, according to the number of the shoot-through bridge arms, the shoot-through states can be divided into three types: single-phase, two-phase and three-phase shoot-through states. The non-shoot-through state refers to all the working states of conventional VSI, including the zero state and the active state.

In the shoot-through state, the cathode voltage of the diode associated with the qZSI network is higher than the anode voltage and the qZSI's inductor is charged by the capacitor, as shown in Fig. 3(a). The shoot-through state equation is expressed as:

$$\begin{cases} L\dot{i}_{L1} = V_{in} + v_{C1} - (r_L + r_C) i_{L1} \\ L\dot{i}_{L2} = v_{C2} - (r_L + r_C) i_{L2} \\ C\dot{v}_{C1} = -i_{L1} \\ C\dot{v}_{C2} = -i_{L2}, \end{cases} \quad (2)$$

where r_L is inductor equivalent resistance; r_C is capacitor equivalent internal resistance.

In the zero state of the non-shoot-through state, the load is disconnected from the impedance network and two sets of charge and discharge circuits are also formed, as shown in Fig. 3(b). Then the zero-state equation can be expressed as:

$$\begin{cases} L\dot{i}_{L1} = V_{in} - v_{C2} - (r_L + r_C) i_{L1} \\ L\dot{i}_{L2} = -v_{C1} - (r_L + r_C) i_{L2} \\ C\dot{v}_{C1} = i_{L2} \\ C\dot{v}_{C2} = i_{L1}. \end{cases} \quad (3)$$

In the active state of the non-shoot-through state, the diode is turned on and the impedance network is connected to the

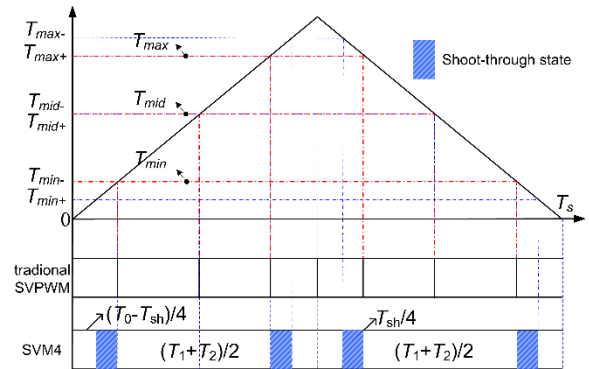


FIGURE 4. Vector distribution of SVM4.

load to supply power, as shown in Fig. 3(c). The active state equation is expressed as:

$$\begin{cases} L\dot{i}_{L1} = V_{in} - r_L i_{L1} - r_C (i_{L1} - i_{load}) - v_{C2} \\ L\dot{i}_{L2} = -r_L i_{L2} - r_C (i_{L2} - i_{load}) - v_{C1} \\ C\dot{v}_{C1} = i_{L2} - i_{load} \\ C\dot{v}_{C2} = i_{L1} - i_{load}. \end{cases} \quad (4)$$

With the state space averaging method, the transfer functions from the shoot-through ratio to the DC-link voltage $G_{v_{pn}/ds}$ and the inductor current $G_{i_{L}/ds}$ are expressed as (5)–(7), as shown at the bottom of the next page: where R is the resistance equivalent to the defined normal power.

III. MODULATION METHODS

A. CONTROL OF BRIDGE ARM SWITCHES

In the modulation, in order to improve the DC-link voltage utilization and reduce the inductor current ripple, the strategy of four-segment SVPWM (SVM4) modulation [25] is adopted, as shown in Fig. 4. In a control cycle, as for SVM4, the total shoot-through time is divided into four equal parts and added into the traditional zero-state vector.

In Fig. 4, T_{sh} indicates the total shoot-through time. T_{max} , T_{mid} and T_{min} are the same to that of the traditional SVPWM and respectively denote the maximum, medium and minimum switching times for the bridge arms. The subscripts of “+” and “-” are used to distinguish the switching times of the upper and lower arm switches. For example, T_{max+} is the conduction time of phase x (x = A, B or C) upper switch and T_{max-} is the blocking time of the same phase lower switch. The switching times are expressed as:

$$\begin{cases} T_{max+} = T_{max} \\ T_{max-} = T_{max} + \frac{T_{sh}}{4} \end{cases} \quad \begin{cases} T_{mid+} = T_{mid} \\ T_{mid-} = T_{mid} \end{cases} \\ \begin{cases} T_{min+} = T_{min} - \frac{T_{sh}}{4} \\ T_{min-} = T_{min} \end{cases} \end{cases} \quad (8)$$

B. CONTROL OF QUASI-Z-SOURCE NETWORK SWITCH

To avoid abnormal working conditions and make sure the qZSI can work under the conditions with significant load

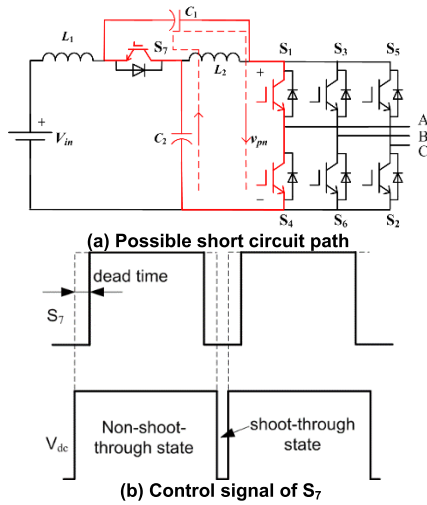


FIGURE 5. Dead time for preventing short circuit.

variations, it is necessary to add an anti-parallel switch S_7 to the quasi-Z-Source diode. The control signal of S_7 is complementary to the shoot-through signal of the inverter [26]–[28]. In other words, S_7 is turned off in the shoot-through state and turned on in the non-shoot-through state. However, in the shoot-through state, if the anti-parallel switch is not reliably turned off, the quasi-Z-Source network capacitor will form a shoot-through loop via the shoot-through bridge arm, as indicated by the dashed arrow in Fig. 5 (assuming that the A-phase bridge arm is in a shoot-through state). This shoot-through loop generates a huge current impact on the capacitor and the bridge arm, which may destroy the IGBTs.

To avoid such safety threats, it is necessary to add dead time into the drive of the anti-parallel switch S_7 . The addition of dead time can be implemented by software or hardware depending on the adopted control chip. In this study, the RC delay circuit was constructed with the external hardware. The generated control signal of S_7 is shown in Fig. 5.

IV. QZSI CONTROLLER DESIGN

The transfer function from shoot-through ratio to the DC-link voltage involves the right half-plane zero point and indicates a non-minimum phase system. The DC-link voltage closed loop system adopts a double-loop control structure with the inductor current as the inner loop and the DC-link voltage as the outer loop, as shown in Fig. 6. The designed cutoff frequency of the outer DC-link voltage loop should

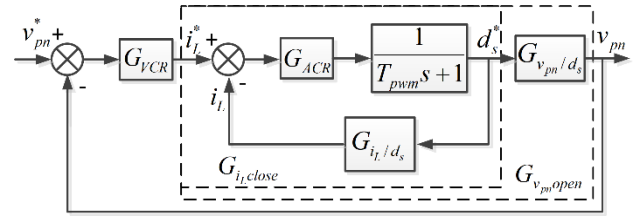


FIGURE 6. DC-link voltage closed loop control system.

be much smaller than the corner frequency of the right half-plane zero point. The design can avoid the influence of the non-minimum phase system on the stability of the system. In addition, the cutoff frequency of the DC side should be less than that of the AC side in order to reduce the coupling interference.

In the controller design, the qZSI and PMSM parameters are given as follows: DC input voltage $V_{in} = 220$ V; switching frequency $f_s = 10$ kHz; PMSM: rated DC-bus voltage = 300 V; rated torque $T_N = 15$ N · m; rated speed = 1500 r/min; pole pairs number $p = 4$.

In qZSI network design, the capacitance and inductance are determined as [27]:

$$L \geq \frac{V_c d_s}{2 \Delta i_L f_s} = \frac{V_c d_s}{2 k_i I_L f_s}, \quad (9)$$

$$C \geq \frac{I_L d_s}{2 \Delta V_c f_s} = \frac{I_L d_s}{2 k_c V_c f_s}, \quad (10)$$

where Δi_L is the inductor current ripple; k_i is the current ripple coefficient; ΔV_c is the capacitor voltage ripple; k_c is the voltage ripple coefficient.

Supposing that the motor works in the rated situation (torque $T = 15$ N · m, speed $n = 1500$ r/min) and the DC-link voltage is boosted to 300 V, then d_s , V_c and I_L can be calculated as:

$$\begin{cases} V_{dc} = \frac{1}{1 - 2d_s} V_{in} \\ V_{c2} = \frac{d_s}{1 - 2d_s} V_{in} \\ V_{c1} = \frac{1 - d_s}{1 - 2d_s} V_{in} \\ I_L = \frac{T \cdot n}{9.55 V_{in}} \end{cases} \quad (11)$$

With the current ripple coefficient $k_i = 20\%$ and the voltage ripple coefficient $k_c = 1\%$, we can get $L \geq 0.43$ mH and $C \geq 178$ μ F. Thus, the design is determined as: quasi-Z-Source network inductor $L_1 = L_2 = L = 0.5$ mH; network

$$G_{v_{pn}/d_s} = \frac{\hat{v}_{pn}}{\hat{d}_s} = 2 \frac{(v_{C1} + v_{C2} - R i_{load})(1 - 2d_s) + (i_{load} - 2i_L)(Ls + r_C + r_L)}{LCs^2 + C(r_C + r_L)s + (1 - 2d_s)^2}, \quad (5)$$

$$G_{i_L/d_s} = \frac{\hat{i}_L}{\hat{d}_s} = \frac{(v_{C1} + v_{C2} - R i_{load})Cs - (i_{load} - 2i_L)(1 - 2d_s)}{LCs^2 + C(r_C + r_L)s + (1 - 2d_s)^2}, \quad (6)$$

$$G_{v_{pn}/i_o} = \frac{\hat{v}_{pn}}{\hat{i}_o} = 2(1 - d_s) \frac{R(1 - 2d_s) - (Ls + r_C + r_L)}{LCs^2 + C(r_C + r_L)s + (1 - 2d_s)^2}, \quad (7)$$

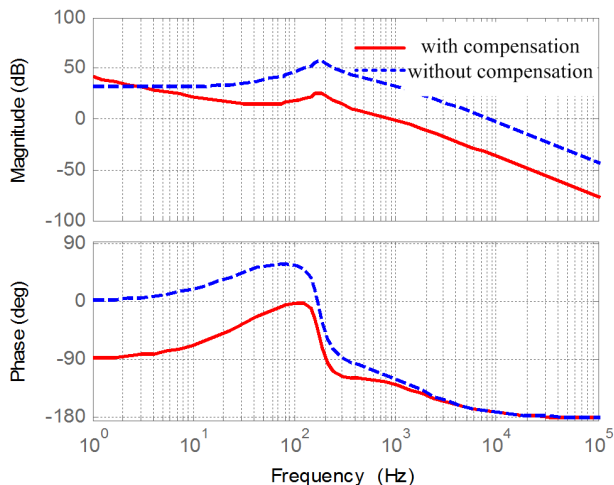


FIGURE 7. Bode diagram of inductor current loop.

capacitor $C_1 = C_2 = 500 \mu\text{F}$; inductor equivalent resistance $r_L = 400 \text{ m}\Omega$; capacitor equivalent internal resistance $r_C = 1 \text{ m}\Omega$.

The same parameters were adopted in simulation tests.

A. FEEDBACK CONTROL

The non-compensated open loop transfer function of the inductor current G_{iLopen} is expressed as:

$$G_{iLopen} = \frac{G_{iL/ds}}{T_{PWMs} + 1}, \tag{12}$$

where T_{pwm} is the switching cycle, $T_{pwm} = 1e-4 \text{ s}$.

When the motor works in the rated condition, the above parameters can be calculated as $i_{load} = T * n/9.55/V_{dc} = 7.85 \text{ A}$ and $R = V_{dc}/i_{load} = 38.2 \Omega$. After substituting these parameters into Eq. (6) and Eq. (12), the non-compensated bode diagrams (Fig. 7) can be plotted based on Eq. (12). The phase margin of the non-compensated open current loop is 11° and the corner frequency is 10 kHz.

If the compensated phase margin increased to 54° and the corner frequency of the current loop decreased to 1 kHz, the system stability was improved and high frequency noise was more significantly suppressed. Therefore, the PI regulator of current loop G_{ACR} can be designed by MATLAB as:

$$G_{ACR} = 0.02 + \frac{20}{s}. \tag{13}$$

The non-compensated open loop transfer function of the DC-link voltage $G_{vpmopen}$ is expressed as:

$$G_{vpmopen} = G_{iLclose}G_{vpm/ds}, \tag{14}$$

where $G_{iLclose}$ is the close loop transfer function of the inductor current.

From Fig. 6, we get

$$G_{iLclose} = \frac{G_{ACR}}{T_{PWMs} + G_{ACR}G_{iL/ds} + 1}. \tag{15}$$

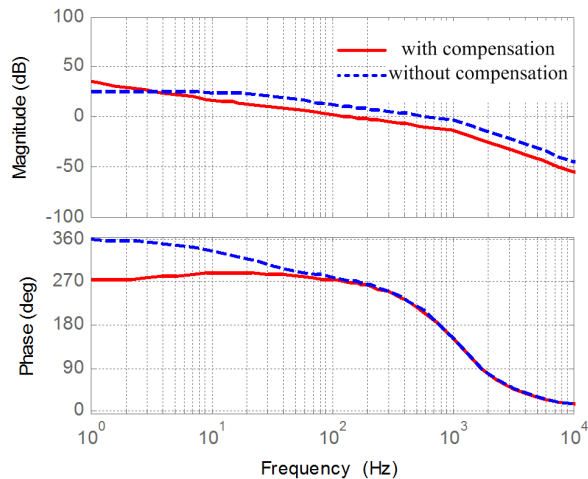


FIGURE 8. Bode diagram of DC-link voltage loop.

With the obtained parameters and Eq. (6), we can get the non-compensated bode diagrams shown in Fig. 8. The gain margin and phase margin of the non-compensated open voltage loop is 1.57 dB and 20.7°, respectively. The corner frequency is 916 Hz.

If the compensated gain margin of the system was changed to 12 dB, the phase margin increased to 89.9° and the corner frequency of the current loop decreased to 205 Hz. Then the PI regulator of voltage loop G_{VCR} can also be designed by MATLAB as:

$$G_{VCR} = 0.3 + \frac{20}{s}. \tag{16}$$

The coupling with the AC side was decreased to avoid the interference of non-minimum phase links. In this way, the anti-interference performance of the control system was improved.

B. COMPOUND CONTROL

The changes in load current and input voltage can cause disturbances in the DC-link voltage. In complex working conditions, such as electric vehicle operating environment, the changes in load power cause the particular disturbance to the DC-link voltage. Even the voltage feedback closed loop cannot ensure the good dynamic response and steady-state accuracy. In order to suppress the disturbance of the load power variation, power feedforward correction is generally added into the voltage feedback control to form a compound control system, as shown in Fig. 9.

The addition of the feedforward control does not affect the designed feedback controller parameters. If the feedforward control is properly designed, it can be approximately considered that the power disturbance is completely offset. However, it should be noted that the feedforward control is an optimization method of the feedback system. If there is only the feedforward control adopted in the system, it is impossible to obtain good control effects and may cause the system instability. The transfer function from load power to

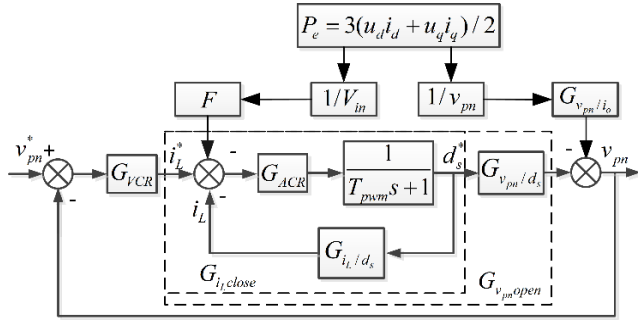


FIGURE 9. Block diagram of a compound control system of the DC-link voltage.

the DC-link voltage before feedforward correction $G_{v_{pn}/pe}$ is expressed as:

$$G_{v_{pn}/P_e} = \frac{G_{v_{pn}/i_o}/v_{pn}}{1 + G_{VCR}G_{v_{pn}/open}}, \quad (17)$$

where G_{v_{pn}/i_o} is the transfer function from load current to the DC-link voltage and can be obtained with Eq. (7).

The transfer function from load power to the DC-link voltage after feedforward correction $G'_{v_{pn}/pe}$ is expressed as:

$$G'_{v_{pn}/P_e} = \frac{G_{v_{pn}/i_o}/v_{pn} - F \cdot G_{v_{pn}/open}/V_{in}}{1 + G_{VCR}G_{v_{pn}/open}}, \quad (18)$$

where F is the disturbance from power to the DC-link voltage. If the system meets Eq. (18), the disturbance can be completely eliminated:

$$F = \frac{V_{in}G_{v_{pn}/i_o}}{v_{pn}G_{v_{pn}/open}}. \quad (19)$$

With the obtained parameters and Eqs. (7), (14) and (19), the final feedforward regulator F is designed as:

$$F = \frac{0.06s + 24}{-0.06s + 432}. \quad (20)$$

Fig. 10 shows amplitude-frequency characteristic curves of the transfer functions from load power to DC-link voltage before and after feedforward correction. Obviously, after the feedforward correction was added, the amplitude gain of the transfer function decreased in the low frequency band, indicating that the feedforward correction enhanced the system capacity to suppress power disturbances and improved the dynamic characteristics.

Fig. 11 shows the simulation waveforms of the load current step under the feedback control and compound control modes. The waveforms from top to bottom are the peak value of the DC-link voltage \hat{v}_{pn} , inductor current and phase current waveforms, respectively. The DC-link voltage v_{pn} is discontinuous. However, its peak value \hat{v}_{pn} is continuous.

At 0.04 s, the load increased suddenly from 3 N · m to 15 N · m and the phase current amplitude increased from 3 A to 15 A. The quasi-Z-Source network inductor current was about 10.7 A. In addition, the DC-link voltage was decreased. In this dynamic process, the DC-link voltage was decreased by 25 V (Fig. 11(a)) under the feedback control method, but

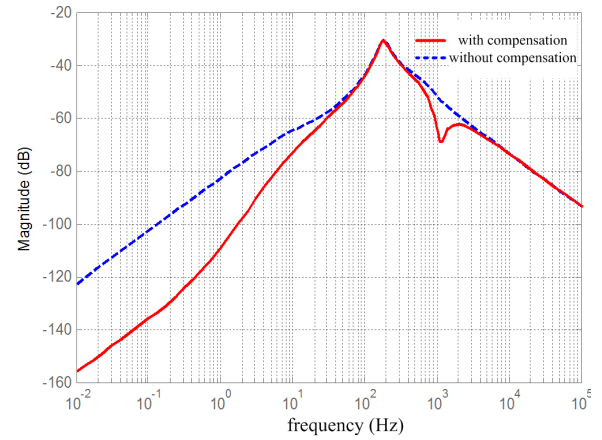
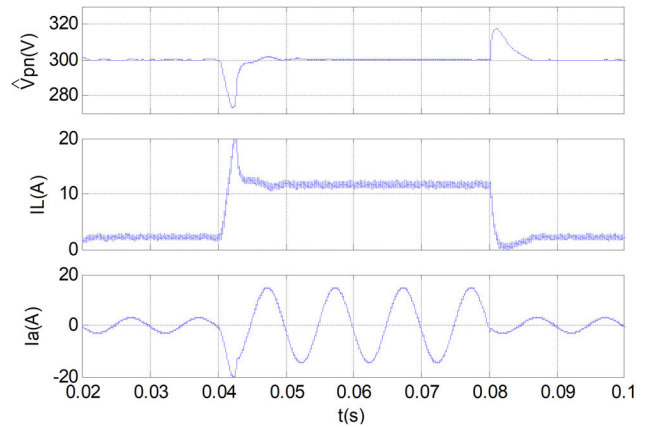
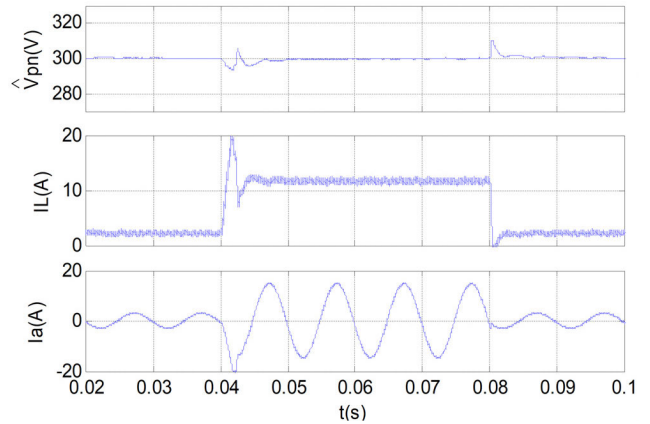


FIGURE 10. Bode diagram of feedforward power loop.



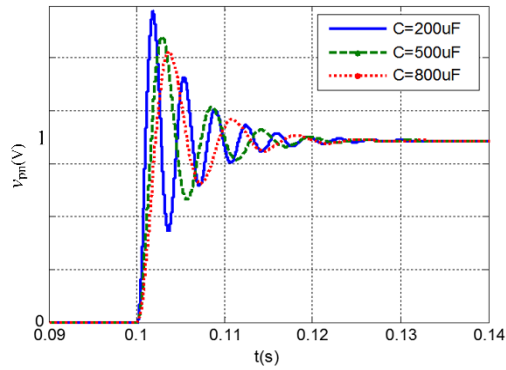
(a) Feedback control.



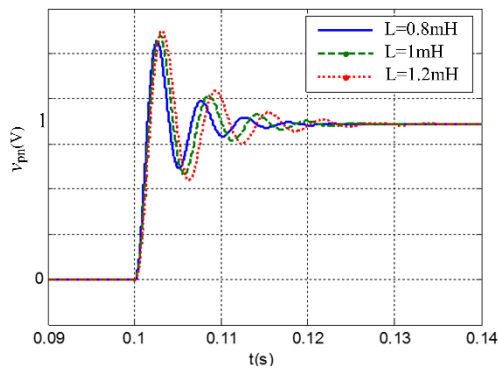
(b) Compound control.

FIGURE 11. Simulation waveforms of load current step response.

the fluctuation under the compound control method was only 5 V (Fig. 11(b)), indicating that the compound control method could compensate for the voltage drop well. At 0.08 s, the load was suddenly reduced and the phase current amplitude was decreased from 15 A to 3 A when the impedance network was instantaneously charged. In addition, the DC-link voltage was increased. The DC-link voltage was increased by 18 V under the feedback control method and increased by

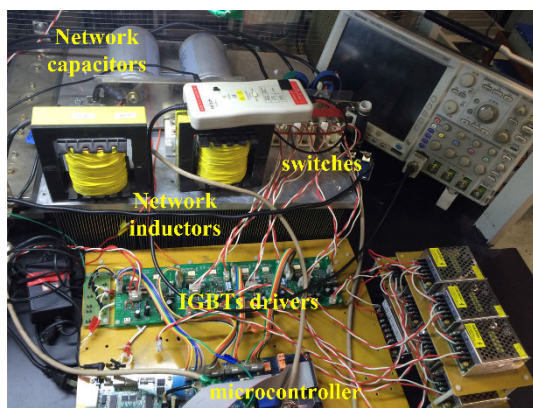


(a) Different capacitors.



(b) Different inductors.

FIGURE 12. Unit step response curves of DC-link voltage with different C (a) and L (b).



(a) QZSI



(b) Motors

FIGURE 13. Experimental setup.

10 V under the compound control method, indicating that the compound control could eliminate the voltage rise well.

At 0.1 s, the shoot-through ratio varied from 0.1 to 0.11. When the network capacitor was changed from

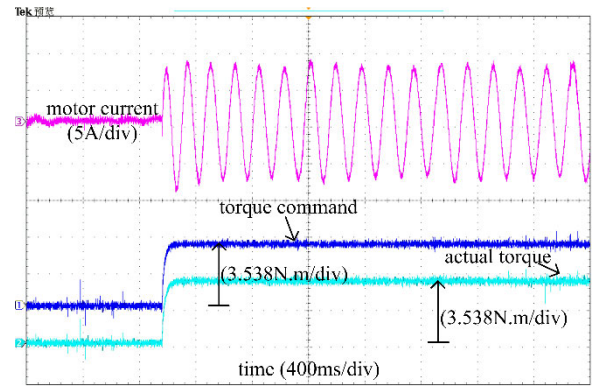


FIGURE 14. Experimental waveforms of torque response @0.25TN.

200 μF to 800 μF and the network inductor increased from 0.8 mH to 1.2 mH, the unit step response curves of DC-link voltage were obtained (Fig. 12). With the increase in the capacitance, the overshoot decreased, but the response time remained unchanged. With the increase in the inductance, both the overshoot and response time increased.

V. MOTOR CONTROLLER DESIGN

The motor side adopted the vector control of $i_d = 0$ and a current-speed double closed-loop control. The motor current signal was obtained by two Hall current sensors and the speed signal was obtained by an encoder. The current and speed controllers were considered based on the traditional PMSM vector control method. The PI controller transfer functions are finally designed as follows:

$$G_{current} = 0.6 + \frac{1}{0.06s}, \quad (21)$$

$$G_{speed} = 4 + \frac{1}{0.008s}, \quad (22)$$

where $G_{current}$ and G_{speed} are the current and speed transfer function, respectively.

The corner frequency of the DC-link voltage loop was set to be lower than that of the motor current loop.

VI. EXPERIMENTAL RESULTS

To verify the proposed compound control strategy, the parameters of the qZSI and PMSM were designed below:

DC input voltage $V_{in} = 200 \text{ V}$; switching frequency $f_s = 10 \text{ kHz}$; PMSM: rated speed $n_N = 2000 \text{ r/min}$; rated torque $T_N = 23 \text{ N} \cdot \text{m}$; rated current $i_N = 20.3 \text{ A}$. According to Eq. (10), the quasi-Z-Source network capacitor voltage and inductor current should meet: $V_c \geq 250 \text{ V}$ and $I_L \geq 24 \text{ A}$. According to Eqs. (8) and (9), the quasi-Z-Source network capacitor and inductor should also meet $L \geq 0.43 \text{ mH}$ and $C \geq 200 \mu\text{F}$. Finally, we designed the quasi-Z-Source network inductor $L_1 = L_2 = L = 1 \text{ mH}/35 \text{ A}$ and chose the network capacitor to be $C_1 = C_2 = C = 500 \mu\text{F}/450 \text{ V}$.

The experimental setup is shown in Fig. 13. Two electrical machines were connected together to drive each other in order to enable the PMSM to work as a motor or a generator. A torque meter was installed in the middle

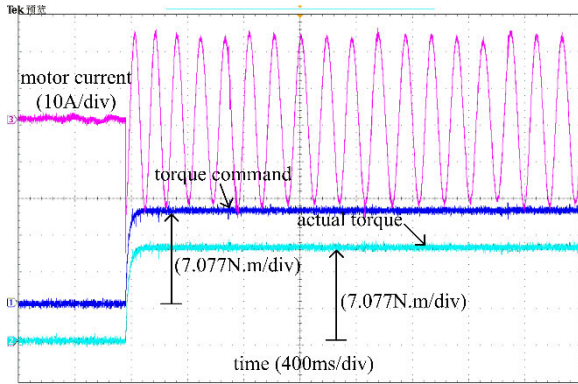


FIGURE 15. Experimental waveforms of torque response @0.8TN.

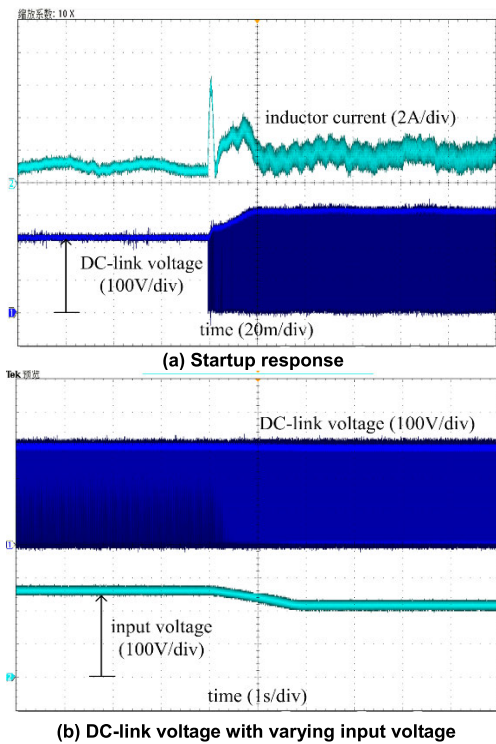


FIGURE 16. Transient waveforms of the qZSI.

of the two machines to measure the PMSM torque and speed. The power circuit switches of the qZSI adopted IGBTs (Infineon BSM50GB60DLC). The microcontroller was DSP2812, on which both the PWM and control strategies were implemented.

The torque was respectively set as 0.25 times and 0.8 times of rated torque (23 N · m). Then, the steady response characteristics of the motor could be observed (Fig. 14 and Fig. 15).

The given i_q^* is displayed in dark blue; the feedback current i_q is displayed in green; the phase current i_a is displayed in light blue. Here, i_q was calculated and measured from DSP2812 D/A signal output. According to the measurements, current loop response time was 2.5 ms under 0.25 times of rated torque. Under 0.8 times of rated torque, current loop response time was 4.1 ms without overshoot, indicating a good motor dynamic characteristics.

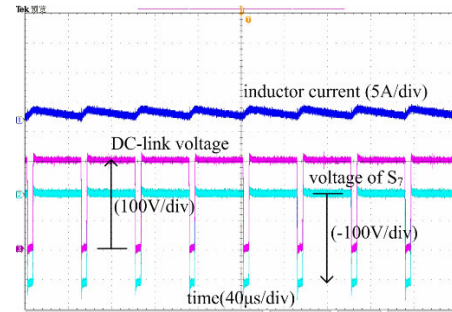


FIGURE 17. Waveforms of the qZSI in carrier cycle.

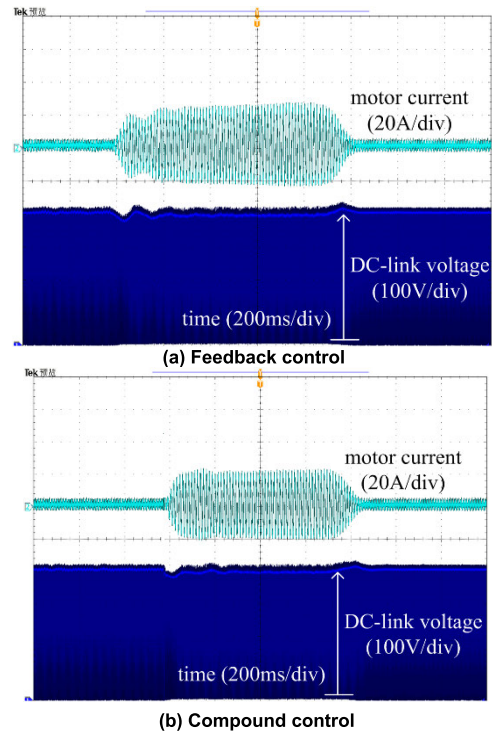


FIGURE 18. DC-link voltage under load disturbance.

Fig. 16(a) shows the startup waveform of the qZSI. The DC-link voltage increased from 230 V to 300 V without an overshoot and response time was 18 ms. At the startup, the inductor current regulator was saturated and the inductor current was overshoot. Subsequently, the regulator was desaturated and the inductor current gradually reached a steady-state balance. When the input voltage dropped from 270 V to 200 V, the DC-link voltage remained at 300 V (Fig. 16(b)).

Fig. 17 shows the steady state waveforms of the qZSI in carrier cycle. The voltage of S_7 was complementary to the DC-link voltage of the inverter. When the DC-link voltage was equal to 300 V, the voltage of S_7 was zero. When the DC-link voltage was 0 V, the voltage of S_7 was equal to -300 V.

Fig. 18 shows the comparison of the waveforms under the two control strategies. The DC-link voltage was set at 200 V

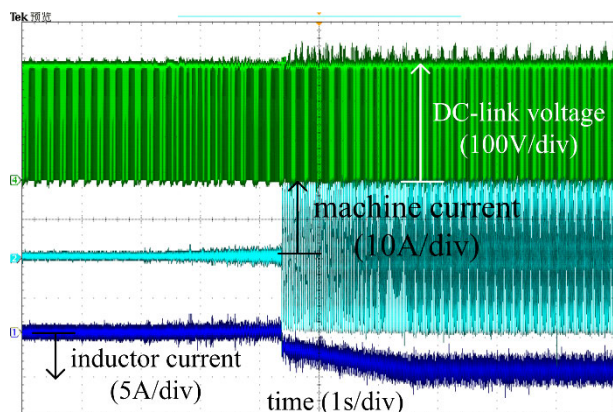


FIGURE 19. Waveforms under braking condition.

and the motor speed was maintained at 1200 r/min. The phase current amplitude firstly increased from 4 A to 20 A and then decreased to 4 A. Under the feedback control mode (Fig. 18(a)), the DC-link voltage fluctuated around 200 V and the fluctuation range was from 187 V to 210 V. Under the compound control mode (Fig. 18(b)), the DC-link voltage fluctuated around 200 V and the fluctuation range was from 192 V to 205 V. The results proved that the compound control strategy had the stronger suppression effect on the fluctuation of DC-link voltage.

In Fig. 19, the machine's speed and torque are in the opposite directions, so that it works under braking conditions. The DC-link voltage and generator speed was set at 280 V and 800 r/min, respectively. The generator torque increased from 0 to 13.8 N · m slowly. The machine current amplitude was about 19.5 A while the quasi-Z-Source inductor current was maintained at -5 A. The input DC voltage was 200 V and the braking power was calculated as 1 kW.

VII. CONCLUSION

In this study, we designed a permanent magnet synchronous motor drive system based on the qZSI. The small-signal model of qZSI and the modulation methods of power circuit IGBTs were established. In addition, we designed the qZSI and motor PI regulators. A novel compound control strategy was proposed in the study. The DC-link voltage showed the good dynamic characteristics under the changes in the startup voltage, input voltage and load current. Load step simulation tests and experiments proved that the compound control system could suppress the fluctuation of DC-link voltage better than the DC-link voltage feedback control system. In the compound control system, the DC-link fluctuation range was from 192 V to 205 V. In the feedback control system, the fluctuation range was from 187 V to 210 V. Experimental results also proved that the designed system could work well under braking conditions.

REFERENCES

[1] S. Dhara, S. Jain, and V. Agarwal, "RES and battery fed energy efficient single-phase induction motor drive system with retrofit solution," *IET Electr. Power Appl.*, vol. 13, pp. 332–339, Mar. 2019.

[2] Z. Pan, S.-Y. Shieh, and B. Li, "Battery state-of-charge pulse-and-glide strategy development of hybrid electric vehicles for VTS motor vehicle challenge," in *Proc. IEEE Vehicle Power Propuls. Conf. (VPPC)*, Aug. 2018, pp. 1–7.

[3] Y. Cao, T. Shi, X. Li, W. Chen, and C. Xia, "A commutation torque ripple suppression strategy for brushless DC motor based on diode-assisted buck-boost inverter," *IEEE Trans. Power Electron.*, vol. 34, no. 6, pp. 5594–5605, Jun. 2019.

[4] A. Guha and G. Narayanan, "Impact of undercompensation and overcompensation of dead-time effect on small-signal stability of induction motor drive," *IEEE Trans. Ind. Appl.*, vol. 54, no. 6, pp. 6027–6041, Nov./Dec. 2018.

[5] A. Guha and G. Narayanan, "Impact of dead time on inverter input current, DC-link dynamics, and light-load instability in rectifier-inverter-fed induction motor drives," *IEEE Trans. Ind. Appl.*, vol. 54, no. 2, pp. 1414–1424, Mar./Apr. 2018.

[6] F. Z. Peng, "Z-source inverter," *IEEE Trans. Ind. Appl.*, vol. 39, no. 2, pp. 504–510, Mar./Apr. 2003.

[7] W. Qian, F. Z. Peng, and H. Cha, "Trans-Z-source inverters," *IEEE Trans. Power Electron.*, vol. 26, no. 12, pp. 3453–3463, Dec. 2011.

[8] P. C. Loh, D. Li, and F. Blaabjerg, "ΓZ-source inverters," *IEEE Trans. Power Electron.*, vol. 28, no. 11, pp. 4880–4884, Nov. 2013.

[9] M.-K. Nguyen, Y.-C. Lim, and Y.-G. Kim, "TZ-source inverters," *IEEE Trans. Ind. Electron.*, vol. 60, no. 12, pp. 5686–5695, Dec. 2013.

[10] M.-K. Nguyen, Y.-C. Lim, and G.-B. Cho, "Switched-inductor quasi-Z-source inverter," *IEEE Trans. Power Electron.*, vol. 26, no. 11, pp. 3183–3191, Nov. 2011.

[11] M. Zhu, K. Yu, and F. L. Luo, "Switched inductor Z-source inverter," *IEEE Trans. Power Electron.*, vol. 25, no. 8, pp. 2150–2158, Aug. 2010.

[12] J. Anderson and F. Z. Peng, "Four quasi-Z-source inverters," in *Proc. IEEE Power Electron. Spec. Conf.*, Jun. 2008, pp. 2743–2749.

[13] M. Muhammad, Z. Rasin, A. Jidin, A. M. Razali, and N. A. Yusoff, "Investigation on quasi-Z-Source inverter with hybrid energy storage for PMSM drive system," in *Proc. 5th IET Int. Conf. Clean Energy Technol. (CEAT)*, 2018, pp. 1–7.

[14] A. Bakeer and A. A. Ahmed, "Performance evaluation of PMSM based on model predictive control with field weakening operation and bidirectional quasi Z-Source inverter," in *Proc. 19th Int. Middle East Power Syst. Conf. (MEPCON)*, Dec. 2017, pp. 741–746.

[15] A. Ayad, P. Karamanakos, R. Kennel, and J. Rodríguez, "Direct model predictive control of bidirectional quasi-Z-Source inverters fed PMSM drives," in *Proc. 11th IEEE Int. Conf. Compat., Power Electron. Power Eng. (CPE-POWERENG)*, Apr. 2017, pp. 671–676.

[16] A. Battiston, J.-P. Martin, E.-H. Miliani, B. Nahid-Mobarakkeh, S. Pierfederici, and F. Meibody-Tabar, "Control of a PMSM fed by a Quasi Z-Source inverter based on flatness properties and saturation schemes," in *Proc. 15th Eur. Conf. Power Electron. Appl. (EPE)*, Sep. 2013, pp. 1–10.

[17] S. Xiao, T. Shi, X. Li, Z. Wang, and C. Xia, "Single-current-sensor control for PMSM driven by quasi-Z-source inverter," *IEEE Trans. Power Electron.*, vol. 34, no. 7, pp. 7013–7024, Jul. 2019.

[18] H. Liu, P. Liu, and Y. Zhang, "Design and digital implementation of voltage and current mode control for the quasi-Z-source converters," *IET Power Electron.*, vol. 6, pp. 990–998, May 2013.

[19] G. Sen and M. E. Elbuluk, "Voltage and current-programmed modes in control of the Z-source converter," *IEEE Trans. Ind. Appl.*, vol. 46, no. 2, pp. 680–686, Mar./Apr. 2010.

[20] Y. Zhang, J. Liu, Z. Dong, H. Wang, and Y.-F. Liu, "Dynamic performance improvement of diode-capacitor-based high step-up DC-DC converter through right-half-plane zero elimination," *IEEE Trans. Power Electron.*, vol. 32, no. 8, pp. 6532–6543, Aug. 2017.

[21] C. J. Gajanayake, D. M. Vilathgamuwa, and P. C. Loh, "Development of a comprehensive model and a multiloop controller for Z-source inverter DG systems," *IEEE Trans. Ind. Electron.*, vol. 54, no. 4, pp. 2352–2359, Aug. 2007.

[22] Y. Tang and S. Xie, "System design of series Z-source inverter with feedforward and space vector pulse-width modulation control strategy," *IET Power Electron.*, vol. 7, no. 3, pp. 736–744, Mar. 2014.

[23] D. Xinping, Q. Zhaoming, Y. Shuitao, and P. Fangzheng, "A new feedforward compensation to reject DC-link voltage ripple in bi-directional Z-Source inverter ASD system," in *Proc. 23rd Annu. IEEE Appl. Power Electron. Conf. Expo.*, Feb. 2008, pp. 1809–1813.

- [24] T. Na, Q. Zhang, and C. Zhou, "Modeling and design of quasi-Z-source inverter for PMSM drive system," in *Proc. UKACC 11th Int. Conf. Control*, Aug./Sep. 2016, pp. 1–5.
- [25] S. Dong, Q. Zhang, and S. Cheng, "Inductor current ripple comparison between ZSVM4 and ZSVM2 for Z-source inverters," *IEEE Trans. Power Electron.*, vol. 31, no. 11, pp. 7592–7597, Nov. 2016.
- [26] S. Dong, Q. Zhang, and S. Cheng, "Analysis of critical inductance and capacitor voltage ripple for a bidirectional Z-source inverter," *IEEE Trans. Power Electron.*, vol. 30, no. 7, pp. 4009–4015, Jul. 2015.
- [27] H. Xu, F. Z. Peng, L. Chen, and X. Wen, "Analysis and design of bi-directional Z-Source inverter for electrical vehicles," in *Proc. 23rd Annu. IEEE Appl. Power Electron. Conf. Expo.*, Feb. 2008, pp. 1252–1257.
- [28] Z. Liang, S. Hu, Y. Liu, W. Li, and X. He, "Application of bi-directional Z-Source in ultracapacitor-battery hybrid energy storage system for EV," in *Proc. IEEE Appl. Power Electron. Conf. Expo. (APEC)*, Mar. 2015, pp. 3124–3127.



DONG SHUAI was born in Shandong, China. He received the Ph.D. degree in electrical engineering from the Harbin Institute of Technology, Harbin, China, in 2016. His research interests include wireless power transfer and power electronics for electric vehicle applications.



ZHANG QIANFAN was born in Heilongjiang, China. He received the B.S. and Ph.D. degrees in electrical engineering from the Harbin Institute of Technology, Harbin, China, in 1999 and 2004, respectively. In 1999, he joined the Department of Electrical Engineering, Harbin Institute of Technology, as a Faculty Member. He has been a Professor, since 2010. His research interests include electric machine and drives, power electronics, electric system on electric vehicle, hybrid electric vehicle, and photovoltaic applications.



ZHANG WEIPAN was born in Hunan, China, in 1994. He received the B.S. degree in electrical engineering from the Harbin Institution of Technology, Harbin, China, in 2018. He is currently pursuing the M.S. degree with the Harbin Institution of Technology. His research interests include wireless power transfer and dc/ac power converters for electric vehicle applications.

ZHOU CHAOWEI received the B.S. degree from the Harbin Institute of Technology, Harbin, China, in 2015. His research interests include electric machine and drives, and power electronics.

NA TUOPU received the B.S. degree from the Harbin Institute of Technology, Harbin, China, in 2014. His research interests include electric machine and drives, and power electronics.

• • •